Graph-Based Optimization of Magnetic Cores for Lightweight and Low-Leakage Inductive Power Transfer Systems

Yaohua Li, *Graduate Student Member, IEEE*, Sicheng Wang, *Student Member, IEEE*, Delin Zhao, *Graduate Student Member, IEEE*, Shuxin Chen, *Member, IEEE*, Yongbin Jiang, *Member, IEEE*, Zhigang Yao, *Senior Member, IEEE*, and Yi Tang, *Senior Member, IEEE*

***Abstract*—Laminated nanocrystalline cores are considered a promising replacement for ferrites in compact and safe inductive power transfer (IPT) systems due to their high saturation flux density and superior shielding capability. However, their inherent anisotropy and high conductivity introduce challenges such as flux discontinuity and eddy current loss, particularly with unipolar coils. Inspired by magnetic core memory structure and leveraging the duality between electric and magnetic circuits, this paper proposes a graph-based evaluation and optimization method to quickly identify critical locations within laminated core plates that hinder flux continuity. By selectively replacing regions that obstruct magnetic flux linkage, eddy current loss is effectively mitigated. Experimental validation on a 3.3 kW IPT prototype demonstrates that the optimized nanocrystalline core configuration achieves 95.71% dc-dc transfer efficiency. The proposed design also reduces weight by 16.3%, leakage flux by 27%, and manufacturing cost by 39.1% compared to a state-of-the-art ferrite core configuration.**

***Index Terms*—Graph theory, inductive power transfer, planar magnetic cores, reluctance distance.**

I. Introduction

INDUCTIVE power transfer (IPT), which enables wireless energy transmission through magnetic coupling between transmitter and receiver coils, has been increasingly used in portable electronic devices [1], [2]. With the penetration of electric vehicles (EVs) in urban transportation and automated guided vehicles (AGVs) in smart factories, this fully automated charging technology has attracted renewed attention in recent years [3], [4], [5].

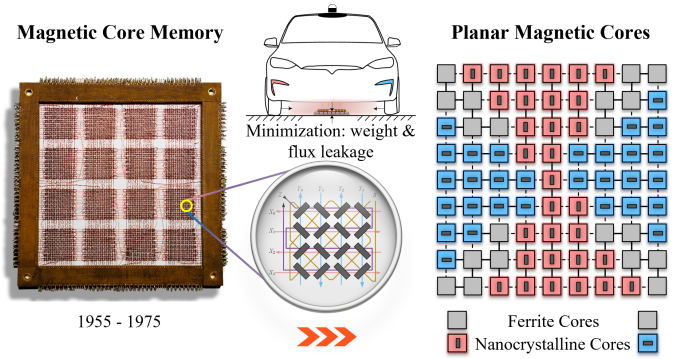

Fig. 1. Transition from magnetic core memory design in computer to planar magnetic core design in inductive power transfer.

Misalignment [6] and metal object detection [7] issues in early EV wireless charging systems have been effectively mitigated through the use of advanced positioning technologies, additional detection coils [8], and automatic tuning circuits [9]. Nevertheless, the bulky installation and magnetic flux leakage of magnetic couplers remain significant challenges in the commercialization of EV wireless chargers (see Fig. 1).

In recent years, nanocrystalline materials have emerged as promising alternatives to ferrites [10], [11], [12] for enhancing the power density of magnetic couplers, thanks to their high saturation flux density [13], [14] and tunable magnetic permeability [15], [16]. Unipolar and bipolar coils are the two most commonly used coil types in high-power wireless charging applications. Typically, unipolar coils outperform bipolar coils in terms of maximum power transfer efficiency and structural simplicity [17], [18], whereas bipolar coils provide better alignment tolerance [19]. The laminated structure of nanocrystalline cores introduces inherent magnetic anisotropy [20], which benefits flux distribution in bipolar coils [21]. However, in unipolar coils, magnetic anisotropy can lead to flux imbalance, thereby reducing system transfer efficiency and compromising safe operation [22], [23]. This makes the design of unipolar coils more challenging, especially when using high-conductivity nanocrystalline materials [24]. To mitigate the eddy current losses caused by the high

Received 6 August 2025; revised 30 October 2025 and 2 December 2025; accepted 30 December 2025. Date of publication XX Month 2026; date of current version XX month 2026. This work was supported in part by A*STAR under its Japan-Singapore Joint Call: Japan Science and Technology Agency (JST) and Agency for Science, Technology and Research (A*STAR) 2024 under Award R24I6IR134 and in part by the Ministry of Education, Singapore, under Grant Tier 1 RG73/24. (*Corresponding authors: Yi Tang; Yongbin Jiang.*)

Yaohua Li, Delin Zhao, Yongbin Jiang, and Yi Tang are with the School of Electrical and Electronic Engineering, Nanyang Technological University, Singapore 639798, Singapore (e-mail: yaohua001@e.ntu.edu.sg; zhao0473@e.ntu.edu.sg; yongbin.jiang@ntu.edu.sg; yitang@ntu.edu.sg).

Sicheng Wang is with the China Electrical Power Research Institute, Beijing 102211, China (e-mail: wangsicheng@epri.sgcc.com.cn).

Shuxin Chen is with the Dyson Singapore Pte. Ltd., Singapore (e-mail: chen1095@e.ntu.edu.sg).

Zhigang Yao is with the State Key Laboratory of Power Transmission Equipment Technology, School of Electrical Engineering, Chongqing University, Chongqing 401331, China (email: zgyao@cqu.edu.cn).

Digital Object Identifier XX.

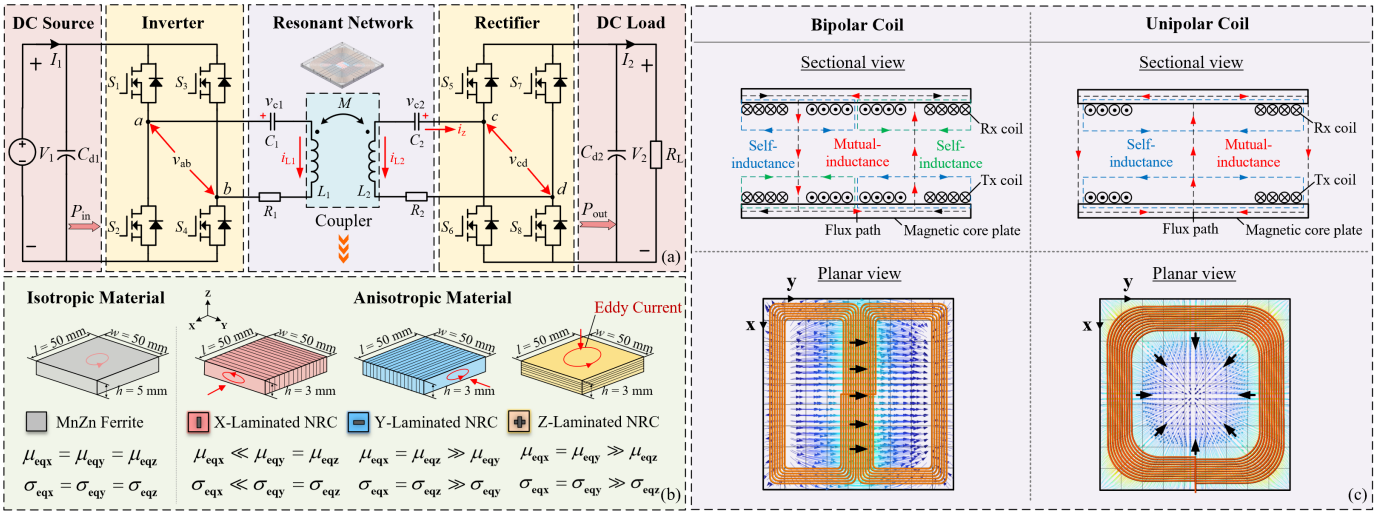

Fig. 2. Fundamentals of magnetic coupler in IPT system. (a) Overview of an IPT system. (b) Classification of magnetic core materials. (c) Spatial flux distribution generated by the bipolar and unipolar coils.

electrical conductivity of these materials, previous studies have employed strategies such as reducing magnetic permeability [25] or segmenting the nanocrystalline ribbon [26]. While effective to some extent, these approaches inevitably degrade the magnetic shielding capability of nanocrystalline materials and increase the manufacturing costs.

This study aims to solve the flux discontinuity and flux imbalance issues caused by the magnetic anisotropy of nanocrystalline materials for unipolar coils. Inspired by the structure of magnetic core memory, which discretizes magnetic materials into interconnected elements, we apply a similar idea to planar IPT cores by representing them as node networks. Leveraging the duality between electric and magnetic circuits, we further introduce the novel concepts of reluctance distance and Magnetic Kirchhoff Index (MKI) from a graph-theoretic perspective to quantitatively evaluate the magnetic flux connectivity and uniformity across different core structures. Our graph-based findings indicate that the dominant factors affecting the figure of merit (FOM) of the magnetic coupler are the magnetic flux connectivity and the uniformity of the magnetic core plate, rather than the high electrical conductivity of the nanocrystalline materials. This insight enables a new design approach for laminated nanocrystalline cores, facilitating wireless charging couplers that balance transfer efficiency, power density, manufacturing cost, and operational safety. The step-by-step derivation process of the reluctance distance and MKI is open-sourced at.[1]

II. Theoretical Analysis

Magnetic cores are indispensable in IPT systems for enhancing the coupling coefficient, and constraining the leakage flux of magnetic couplers. The FOM of the resonant network determines the power transfer capability and efficiency in a series-series (S-S) compensated IPT system [see Fig. 2(a)], which can be expressed as

$$\mathrm{FOM} = \frac{\omega_s k \sqrt{L_1 L_2}}{\sqrt{R_1 R_2}} \tag{1}$$

where L_1 and L_2 are the self-inductances of the transmitter (Tx) and receiver (Rx) coils. R_1 and R_2 are the equivalent series resistance (ESR) of the Tx and Rx coils. ω_s and k are the angular switching frequency and coupling coefficient of the system, respectively.

The material and geometry of magnetic cores affect the FOM of resonant network. Magnetic core materials can be classified into isotropic and anisotropic types [see Fig. 2(b)]. Ferrites exhibit magnetic isotropy due to the random orientation of their grains, whereas laminated nanocrystalline ribbon cores (NRCs) show magnetic anisotropy resulting from grain alignment induced by stress annealing. This structural difference gives isotropic ferrites uniform magnetic permeability and electrical conductivity, whereas anisotropic NRCs exhibit direction-dependent magnetic and electrical properties along three orthogonal axes.

In general, NRCs exhibit higher permeability along the non-laminated axes. Therefore, it is appropriate to place x-laminated NRCs under the bipolar coil, which generates a left-to-right magnetic flux pattern, as indicated in Fig. 2(c). In contrast, the unipolar coil generates a magnetic flux distribution that converges from the periphery toward the center. Placing x-laminated NRCs beneath the unipolar coil will result in a non-uniform magnetic flux distribution.

To optimize the flux connectivity and uniformity of magnetic cores, this section first introduces the novel concept of reluctance distance, and then proposes a multi-port graph-based coupler model to quantitatively evaluate the magnetic flux connectivity and uniformity by calculating the MKI.

A. Reluctance Distance

Resistance distance is a metric in graph theory, derived from electric circuit theory, that quantifies the effective distance

[1][Online]. Available: https://github.com/Yaohua001/TIE

between two nodes in a graph [27]. This concept models the graph as a resistive network, where each edge e is treated as a resistor R, and the resistance distance is defined as the equivalent resistance between two nodes, as indicated in Fig. 3.

This concept was first applied in chemical graph theory to describe molecular structures [28]. Given the duality nature between electric and magnetic circuits, we hypothesize that a duality concept of resistance distance can be applied to magnetic graph theory to characterize magnetic circuit structures, and we term this as "reluctance distance".

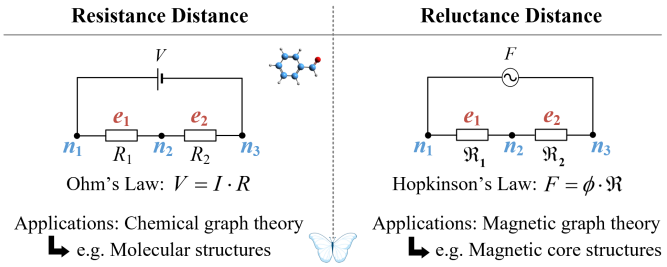

Fig. 3. Duality between electric and magnetic circuits.

However, magnetic circuits are much more complex than electric circuits. In IPT systems, magnetic flux is spatially distributed (see Fig. 4). Therefore, each core's reluctance is decomposed into three orthogonal components in the planar core plate, with its center modeled as a node n (see Fig. 5). In the equivalent magnetic circuit model, the alternating current in the coil creates a magnetomotive force $F_{\mathrm{n},i}$ around the core i, which drives the external magnetic flux $\phi_{\mathrm{n},i}$ into the core. The node i connects to the surrounding node j, forming a flux path weighted by reluctance

$$\Re_{\mathrm{e},ij} = \frac{F_{\mathrm{e},ij}}{\phi_{\mathrm{e},ij}} = \frac{l_i/2}{\mu_0 \mu_{\mathrm{eq}x,i} \cdot S_i} + \frac{l_j/2}{\mu_0 \mu_{\mathrm{eq}x,j} \cdot S_j} \tag{2}$$

where the flux and magnetic potential difference along the path are $\phi_{\mathrm{e},ij}$ and $F_{\mathrm{e},ij}$, respectively. l_i and $S_i = w_i a_i$ are the path length and cross-sectional area of the core i, respectively. w_i and a_i represent the width and thickness of the core i, respectively. μ_0 and $\mu_{\mathrm{eq}x,i}$ denote the vacuum permeability and equivalent relative permeability of the core i in the x-direction, respectively.

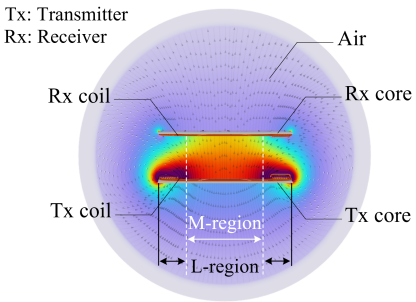

Fig. 4. 3D view of spatial magnetic field distribution for unipolar coil.

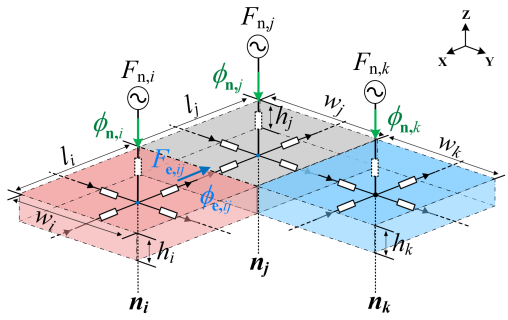

Fig. 5. Schematic of reluctance-based planar magnetic core model.

By applying a graph representation, the core centers are treated as network nodes, and the flux paths are represented as edges connecting them. A graph-based reluctance network is then generated. For example, a directed graph G has 9 nodes and 12 edges, as shown in Fig. 6. The all-node incidence matrix A_{c} of graph G is a 9×12 matrix, where each row corresponds to a node and each column to an edge. The element a_{ij} of the incidence matrix A_{c} is defined as follows:

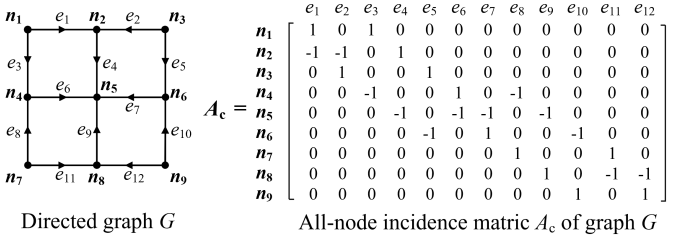

Fig. 6. A directed graph G with 9 nodes and 12 edges.

$$a_{ij} = \begin{cases} 1, & \text{if edge } j \text{ is connected to node } i \\ & \text{and oriented away from it;} \\ 0, & \text{if edge } j \text{ is not connected to node } i; \\ -1, & \text{if edge } j \text{ is connected to node } i \\ & \text{and oriented toward it.} \end{cases} \tag{3}$$

In this model, it is assumed that each node can also serve as a port, with node j designated as the reference node. The relationship between the internal magnetic flux matrix ϕ_{e} and the internal magnetic potential difference matrix F_{e} between two adjacent nodes can be expressed as:

$$\phi_{\mathrm{e}} = W_{\mathrm{e}} F_{\mathrm{e}} \tag{4}$$

where the matrix W_{e} is the diagonal edge-permeance matrix with its entry $w_{\mathrm{e},ij} = 1/\Re_{\mathrm{e},ij}$. The internal magnetic flux matrix ϕ_{e} is connected to the external magnetic flux matrix ϕ_{n} with the following relationship:

$$A\phi_{\mathrm{e}} = \phi_{\mathrm{n}} \tag{5}$$

where $\phi_{\mathrm{n}} = \begin{bmatrix} \phi_{\mathrm{n},1j} & \cdots & \phi_{\mathrm{n},ij} & \cdots & \phi_{\mathrm{n},(n-1)j} \end{bmatrix}^{\mathrm{T}}$.

The elements $\phi_{\mathrm{n},ij}$ in matrix ϕ_{n} denote the external magnetic flux injected from node i to the reference node j. The

matrix A is the submatrix of the full incidence matrix A_c of graph G, obtained by removing the jth row. Accordingly, the relationship between the externally injected magnetomotive force matrix F_n and the internal magnetic potential difference matrix between two adjacent nodes F_e can be calculated as:

$$F_e = A^T F_n \tag{6}$$

where $F_n = \begin{bmatrix} F_{n,1j} & \cdots & F_{n,ij} & \cdots & F_{n,(n-1)j} \end{bmatrix}^T$.

The elements $F_{n,ij}$ in matrix F_n are the difference of injected magnetomotive force between node i and the reference node j. By substituting the (4) and (6) into (5), the following equation can be obtained:

$$AW_e A^T F_n = Y F_n = \phi_n \tag{7}$$

where the matrix Y can be defined as the node-permeance matrix of the multi-port network with node j as the reference node, characterizing the global relationship between magnetic flux and magnetomotive force. It is worth noting that matrix A can be represented in terms of edge vectors a_{ei}, such that $A = [a_{e1}, a_{e2}, \ldots, a_{em}]$ and $Y = \sum_i^m w_{ei}\, a_{ei}\, a_{ei}^T$. Reversing the orientation of any edge only changes the sign of a_{ei}, but not that of $a_{ei}a_{ei}^T$. Therefore, Y is invariant to the orientation of edges in A. According to Cramer's rule, (7) can be further simplified as:

$$F_{n,ij} = \frac{\det(Y_{i\phi})}{\det(Y)} \tag{8}$$

where the matrix $Y_{i\phi}$ is constructed by replacing the ith column of the coefficient matrix Y with the column vector ϕ_n. When magnetic flux is only injected at node i, the determinant of $Y_{i\phi}$ can be further expanded into a cofactor form along the ith column as:

$$F_{n,ij} = \frac{\sum_{k=1}^{n-1} \phi_{n,kj} \cdot \det(Y_{ki})}{\det(Y)} = \phi_{n,ij} \cdot \frac{\det(Y_{ii})}{\det(Y)} \tag{9}$$

where $\det(Y_{ii})$ denotes the determinant of the (i,i) cofactor of the node-permeance matrix Y. Based on (9) and Hopkinson's Law, the reluctance distance between node i and the reference node j can be expressed as:

$$r_{ij} = \frac{F_{n,ij}}{\phi_{n,ij}} = \frac{\det(Y_{ii})}{\det(Y)}. \tag{10}$$

Unlike the conventional shortest-path criterion, reluctance distance accounts for all effective flux paths, enabling a more comprehensive evaluation of flux connectivity and uniformity in planar magnetic cores.

B. Magnetic Kirchhoff Index

In network science, the Kirchhoff Index (KI) quantifies the global connectivity of a graph G and is defined as:

$$\mathrm{KI}(G) = \sum_{i>j} r_{ij} \tag{11}$$

where r_{ij} denotes the effective resistance distance between node i and j. However, this equation cannot be directly used to measure the connectivity of planar magnetic cores because it ignores the following factors:

1) Coil position determines the magnetic field distribution within the core plate.
2) Reluctance model neglects the impact of the material's electrical conductivity on system performance.

To address these limitations, we propose a multi-port graph-based reluctance model for planar magnetic arrays in IPT systems, as shown in Fig. 7. In this model, the magnetic core plate is divided into L-region and M-region nodes based on the coil position. Since the magnetic field is much stronger beneath the coil, the magnetic flux connectivity and uniformity in this region are critical to system performance. Therefore, the nodes directly under the coil are defined as L-region nodes, while those near the coil center are classified as M-region nodes (see Fig. 4 and Fig. 7). M-region nodes provide effective flux linkage with the receiver coil, where all magnetic flux participating in the coupling converges at the lumped node. Due to the requirement for magnetic flux coupling between the Tx and Rx coils, at least one M-region node must exist in the multi-port model.

Furthermore, peripheral nodes are placed along the outermost magnetic cores to evaluate the lateral magnetic flux conduction capability of the core plate. These nodes are especially crucial for anisotropic materials, since magnetic flux entering along the stacking direction of the NRC can generate significant surface eddy current losses due to the material's high electrical conductivity [see Fig. 2(b)]. Considering all nodes in a graph G, the MKI of multi-port graph-based reluctance model is defined as:

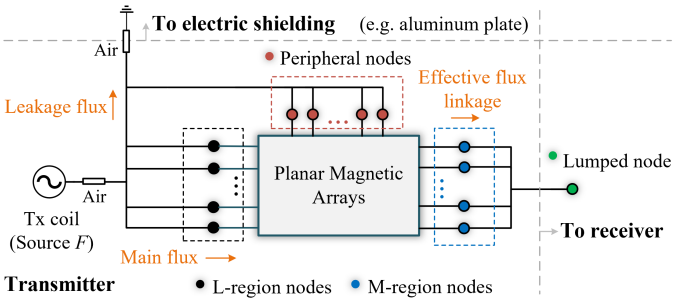

Fig. 7. Proposed multi-port graph-based reluctance model for coupler.

$$\mathrm{MKI}(G) = \frac{1}{\alpha} \cdot \sum_{\substack{i \in \text{ Input nodes} \\ j \in \text{ Lumped node}}} r_{ij} + \frac{1}{\beta} \cdot \sum_{\substack{i \in \text{ Peripheral nodes} \\ j \in \text{M-region nodes}}} r_{ij}. \tag{12}$$

The first term represents the average magnetic reluctance distance from the L-region and peripheral nodes to the lumped node, highlighting the role of flux connectivity in facilitating effective flux coupling between the Tx and Rx coils. The second term represents the average reluctance distance from the peripheral nodes to the M-region nodes, indicating how well the core network attracts and guides magnetic flux uniformly inward from all four sides. The coefficients α and

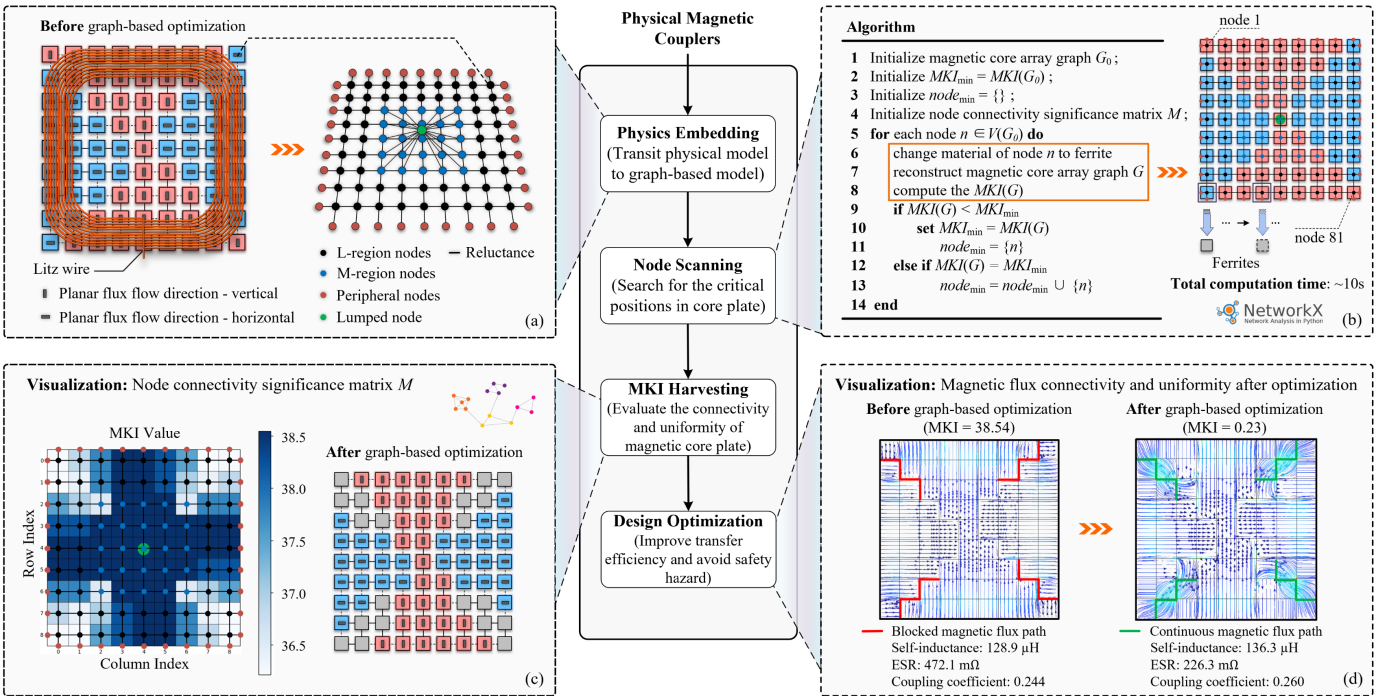

Fig. 8. Flowchart of the proposed graph-based design optimization process driven by reluctance distance and Magnetic Kirchhoff Index. (a) Physics embedding process. (b) Node scanning for critical positions. (c) Visualization of MKI harvesting results. (d) Visualization of magnetic flux connectivity and uniformity before and after optimization.

β respectively indicate the number of magnetic reluctance distances contributing to each superimposed term. Consistent with the definition of the KI in network science, a lower MKI value represents better flux connectivity and uniformity. By optimizing the arrangement of magnetic cores, the MKI value can be significantly reduced, thereby enhancing the connectivity and uniformity of the planar magnetic array as well as the overall FOM of the magnetic coupler. This ultimately enhances both transfer efficiency and safety.

III. Graph-Based Optimization of Magnetic Core Structures

Building on the definitions of reluctance distance and MKI, this section demonstrates their application in evaluating and optimizing magnetic flux connectivity and uniformity.

A. Physics-Embedding of Magnetic Couplers

Benefiting from the proposed multi-port reluctance model, any unipolar coil together with isotropic or anisotropic magnetic cores in an IPT system can be represented as a graph [see Fig. 8(a)]. Following the findings in [23], 81 *x*/*y*-laminated NRCs are arranged in an interleaved pattern beneath a rectangular coil. The 56 L-region nodes located under the coil act as input ports for the coil excitation source, representing the main flux path. The 25 M-region nodes in the central area of the coil are connected to a lumped node that models the flux linkage to the receiver coil, forming the output port. In addition, 36 peripheral nodes also serve as input ports to characterize the magnetic flux conduction capability along the edges of the magnetic core plate. The small magnetic needle in each core indicates the magnetic flux direction, which is governed by the laminated structure of the nanocrystalline material. The parameter α is obtained by $(36 + 56) \times 1 = 92$, while β is calculated as $36 \times 25 = 900$. The same transformation can be applied to other unipolar coil geometries.

B. MKI Harvesting for Magnetic Core Structures

After converting the physical coupler into the graph-based model, the MKI value can be calculated via matrix operations using (12). To identify the most critical positions influencing magnetic flux connectivity, a stepwise search and replacement strategy is applied, as illustrated in Fig. 8(b). In this node scanning process, each core in the plate is sequentially replaced by an isotropic ferrite core, and the corresponding MKI value of the entire core plate is recalculated after each replacement. This approach enables precise identification of the critical magnetic flux pathways within the core plate. Thanks to efficient matrix computation in graph-based network analysis, replacing 81 cores and evaluating their MKI values takes only 10 seconds on an AMD Ryzen 9 7950X CPU.

C. Design Optimization of Magnetic Core Structures

Fig. 8(c) visualizes the calculated MKI values of the node connectivity significance matrix M obtained from the node scanning process. A lower MKI value indicates better flux connectivity after replacing the NRC with ferrite. It should be noted that the most critical positions are located beneath the coils, whereas the cores in the center of the coil region are less sensitive. This is because the magnetic field intensity is much stronger around the coils, which is already reflected in the physical embedding process. Blocking the magnetic flux paths in these regions leads to substantial eddy current

accumulation and may even result in potential safety issues, which will be demonstrated in the later experiments. Fig. 9 shows the optimization procedure for the graph-based model.

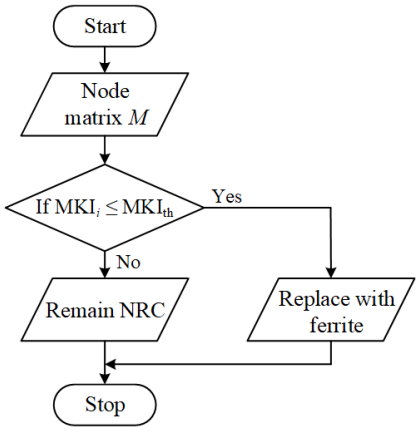

Fig. 9. Optimization procedure for the graph-based model.

The optimization procedure starts from the node connectivity significance matrix M, and the MKI value at each position, denoted as MKI_i, is compared with a user-defined MKI threshold. Nodes with MKI values less than or equal to the threshold are recommended to be replaced with ferrites, while the remaining positions retain NRCs. Designers may adjust this threshold according to efficiency, weight, and cost requirements to determine the appropriate number of replacements. In general, the threshold should ensure that NRCs located under the coil, where magnetic connectivity and uniformity are most critical, are replaced with ferrites. In our study, with the threshold set to 37, a total of 20 NRCs were replaced with ferrites.

To verify the effectiveness of the optimization results, COMSOL simulations are conducted. As shown in Fig. 8(d), the significant reduction in MKI values leads to a substantial improvement in magnetic flux connectivity and uniformity across the magnetic core plate. This directly results in an increase in the measured coil self-inductance (from 128.9 μH to 136.3 μH) and the coupling coefficient (from 0.244 to 0.260). Most importantly, it significantly reduces the ESR of the magnetic coupler (from 472.1 mΩ to 226.3 mΩ). Assuming the same 25 nF resonant capacitor is used for both couplers before and after optimization, the FOMs at their respective resonant frequencies can be calculated according to (1) as 38.62 and 85.10, respectively. These observations highlight the strong impact of magnetic flux connectivity and uniformity on the coupler's FOM. Even though NRC materials have high electrical conductivity, the FOM can still be enhanced through proper core arrangement.

The described procedure offers a fully automated workflow, from model construction and MKI computation to magnetic core distribution optimization. By representing the magnetic coupler as a graph, flux connectivity and uniformity across the core plate can be efficiently quantified using matrix operations. Critical nodes are rapidly identified and selectively replaced with isotropic ferrite cores, improving resonant network parameters and system safety. Our open-source code allows designers to input the core distribution and automatically compute the MKI to evaluate flux connectivity and uniformity.

IV. Experimental Verification

A. Prototype Setup

To verify the proposed concepts and optimization method, six representative core structures (see Fig. 10) are experimentally tested at a vertical transfer distance d_t of 150 mm using the circulating current method. By directly connecting the dc input and output, this approach enables internal power circulation and allows focused evaluation of losses in the magnetic couplers and MOSFETs. Since rectangular and circular coils inherently share a similar magnetic field distribution, their experimental results are similar and comparable. Due to page limitations, this section focuses on experimental results for the rectangular coil, while the methodology has also been validated on the circular coil. The Tx and Rx coils have identical shapes and dimensions, as shown in Fig. 11.

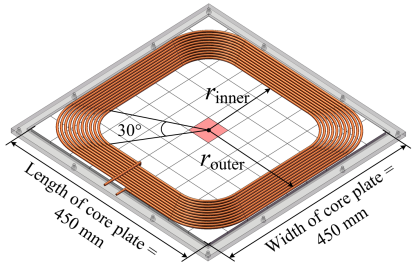

Fig. 11. Dimensions of rectangular coil and magnetic core plate.

Each rectangular coil consists of 11 turns of litz wire, with an inner radius r_{inner} of 158 mm and an outer radius r_{outer} of

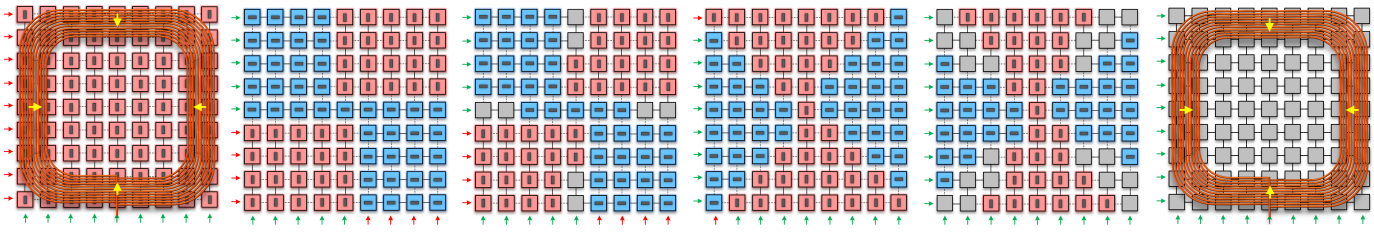

Fig. 10. Comparison of six planar magnetic core configurations. (a) Case 1: full *x*-laminated NRCs. (b) Case 2: unimproved NRCs. (c) Case 2+: improved NRCs with ferrites for case 2. (d) Case 3: unimproved NRCs. (e) Case 3+: improved NRCs with ferrites for case 3. (f) Case 4: full ferrites.

TABLE I
SYSTEM PARAMETERS WITH DIFFERENT CORE STRUCTURES

Symbol	Quantity	Value (Case 1)	Value (Case 2)	Value (Case 2+)	Value (Case 3)	Value (Case 3+)	Value (Case 4)
L_1	Self-inductance of Tx	115.9 μH	124.8 μH	128.7 μH	128.9 μH	136.3 μH	141.6 μH
L_2	Self-inductance of Rx	115.2 μH	122.6 μH	125.8 μH	127.7 μH	134.7 μH	141.5 μH
C_1,C_2	Resonant capacitance	32 nF	25 nF	25 nF	25 nF	25 nF	25 nF
R_1	ESR of Tx	772.1 mΩ	781.5 mΩ	447.4 mΩ	472.1 mΩ	226.3 mΩ	84.4 mΩ
R_2	ESR of Rx	740.8 mΩ	759.4 mΩ	432.1 mΩ	430.8 mΩ	221.9 mΩ	94.3 mΩ
k	Coupling coefficient	0.237	0.241	0.253	0.244	0.260	0.269
f_s	Switching frequency	82.7 kHz	90.0 kHz	88.7 kHz	88.6 kHz	86.2 kHz	84.6 kHz
d_t	Transfer distance	150 mm	150 mm	150 mm	150 mm	150 mm	150 mm
V_1	DC input voltage	268.7 V	275.4 V	277.5 V	270.5 V	288.8 V	283.0 V
P_{out}	Output power	3.3 kW	3.3 kW	3.3 kW	3.3 kW	3.3 kW	3.3 kW
P_{loss}	Total power loss	451.3 W	441.9 W	266.1 W	288.5 W	147.9 W	100.7 W
η_{dc-dc}	DC-DC efficiency	87.97%	88.19%	92.54%	91.96%	95.71%	97.04%
-	Weight of core	3807g	3807g	3911g	3807g	4067g	4860g
-	Cost of core*	$299.7	$299.7	$331.7	$299.7	$379.7	$623.7
FOM	Figure of merit	18.81	21.87	40.78	38.62	85.10	226.76
MKI	Magnetic Kirchhoff Index	45.46	41.79	22.89	38.54	0.23	0.13

* estimated based on the unit price of each core: $3.7 per NRC107B and $7.7 per PC95.

224 mm, respectively. Litz wire is used to minimize high-frequency copper losses caused by the skin and proximity effects, and its detailed specifications are shown in Fig. 12.

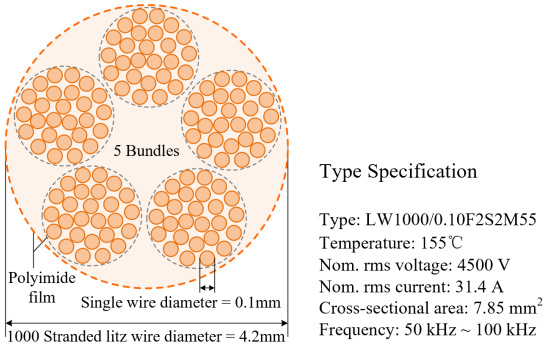

Fig. 12. Construction of litz wire used in this work.

The experimental prototype and hardware setup are shown in Fig. 13. It consists of a bidirectional power supply (IT6006C), a full-bridge inverter and rectifier controlled by microcontroller units (DSP: TMS320F28379D), and power MOSFETs (C3M0021120D). The thermal images are captured by Fluke Ti300+ thermal imaging camera. The temperature measurements were performed using a DagaSensor 12-channel thermocouple thermometer. All system parameters and the dc-dc efficiency listed in Table I were measured using the Wayne Kerr 6500B impedance analyzer and the Yokogawa WT5000 power analyzer, respectively. The MKI values are calculated using the open-sourced code in Python.

To control variables and observe local behaviors, isotropic ferrite PC95 manufactured by TDK [29] and anisotropic NRC107B cores manufactured by Antai [30] are fabricated into small pieces with identical length and width but different thicknesses [see Fig. 2(b)], with the material parameters listed in Table II. NRC107B cores are 2 mm thinner than PC95 cores, taking advantage of the high saturation flux density of

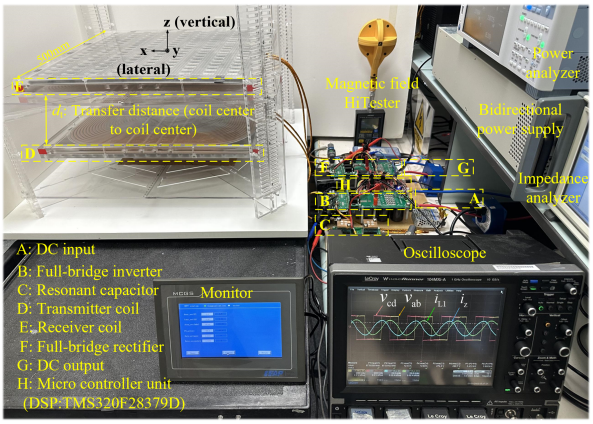

Fig. 13. Experimental prototype with assembled IPT couplers.

TABLE II
PARAMETERS OF MAGNETIC MATERIALS USED IN THIS WORK

Symbol	Quantity	Value
μ_{PC95}	Relative permeability of MnZn ferrite PC95	3300
σ_{PC95}	Conductivity of MnZn ferrite PC95	0.167 S/m
$\mu_{NRC107B}$	Relative permeability of nanocrystalline ribbon core NRC107B	25740* 4.545**
$\sigma_{NRC107B}$	Conductivity of nanocrystalline ribbon core NRC107B	$6.5e^5$ S/m* 34.3 S/m**

* non-laminated directions. ** laminated direction.

NRC materials. Six core distributions shown in Fig. 10 are symmetrically placed in the Tx and Rx magnetic core plates indicated in Fig. 11 to evaluate their performance.

B. Resonant Network Parameters and Transfer Efficiency

In principle, any magnetic core configuration can be represented by our graph-based model, which enables automatic evaluation and optimization of flux connectivity and uniformity through calculation of the MKI value. Six representative cases were used to validate the proposed model, including

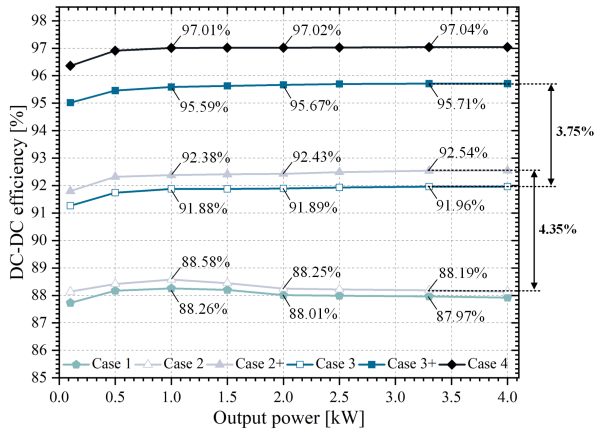

Fig. 14. Measurement results of dc-dc efficiency for the representative core structures under a 15 cm transfer distance.

full x-laminated NRC107B cores (Case 1), unoptimized and optimized NRC107B structures (Cases 2, 2+, 3, and 3+), and full ferrite PC95 cores (Case 4). The self-inductance and ESR of the coil vary depending on the magnetic core configuration. The resonant capacitors with capacitances of 25 nF and 32 nF were assembled from 25/50/85 nF Celem power capacitors (CSP120/200) through appropriate series and parallel configurations for all cases, and the switching frequency was adjusted to ensure the system operated at resonance condition. All cases are evaluated at output power levels up to 4 kW, as shown in Fig. 14. The operating conditions at an output power of 3.3 kW will be analyzed in the following sections. To maintain the same output power of 3.3 kW, the input/output dc voltages were adjusted during the experiments.

First, the effectiveness of MKI in evaluating magnetic flux connectivity can be reflected from Case 2 and 2+. In an IPT magnetic coupler, the magnetic cores with the strongest magnetic flux density are generally located beneath the coil. Connecting the x-laminated NRC cores with the y-laminated NRC cores underneath the coil will disrupt the magnetic flux path. By simply replacing eight NRC cores that obstruct magnetic path connectivity with ferrite cores, the MKI value greatly decreases from 41.79 in Case 2 to 22.89 in Case 2+, as listed in Table II. A reduction in the MKI value indicates improved magnetic path connectivity. For the resonant network parameters, this improvement leads to a slight increase in coil self-inductance and a significant reduction in the coil's ESR. According to (1), the FOM of the magnetic coupler increases from 21.87 in Case 2 to 40.78 in Case 2+. These results clearly demonstrate that magnetic flux connectivity is crucial for determining the coil's ESR. When the magnetic connectivity of the core is poor, the magnetic flux is forced to detour or concentrate in certain regions. Such localized flux concentration not only increases hysteresis losses but also induces strong eddy currents, which are rapidly converted into heat, especially in high-conductivity materials such as nanocrystalline alloys. The increase in these losses manifests as a higher coil ESR in the equivalent circuit. A lower MKI value indicates improved magnetic flux connectivity, which consequently results in a higher FOM. At the system level, the dc-dc efficiency increases by 4.35 percentage points, from 88.19% in Case 2 to 92.54% in Case 2+, as shown in Fig. 14. Similar experimental phenomena are also observed in Case 3 and 3+.

Second, Case 2+ and 3+ demonstrate the importance of magnetic flux uniformity, while ensuring connectivity. The peripheral nodes introduced in our proposed multi-port model enable the MKI to effectively assess the uniformity of magnetic flux entry from the lateral sides of the core plate. In Case 3+, magnetic flux can seamlessly enter the core plate from all four sides. A lower MKI value in Case 3+ indicates improved uniformity, leading to an efficiency of 95.71%. In contrast, half of the magnetic cores on the four sides in Case 2+ lose their ability to attract magnetic flux. When the flux enters along the NRC laminated axes, substantial eddy current losses occur. It should be noted that enhanced uniformity also leads to a higher FOM.

To verify the generalizability of our graph-based methodology, two extreme cases are compared. The MKI value for Case 1 indicates that the unipolar coil is adversely affected by the anisotropy of the NRC material, leading to a significant 9.07 percentage points drop in efficiency compared to Case 4, which uses full PC95 ferrite cores and exhibits the lowest MKI. By optimizing the arrangement of fully NRCs using our proposed method, the magnetic flux connectivity and uniformity of the core plate can be significantly improved. As a result, the dc-dc efficiency of the NRC-dominated core plate is enhanced by 7.74 percentage points, reaching 95.71%.

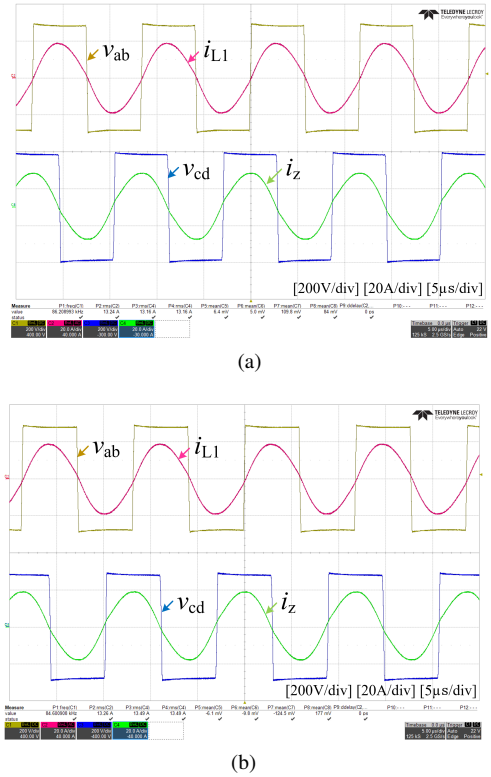

Fig. 15. Operation waveforms of Case 3+ and Case 4 at 3.3 kW output power. (a) Case 3+. (b) Case 4.

Fig. 15 shows the operational waveforms of Case 3+ and Case 4 at 3.3 kW output power. Although Case 3+ still

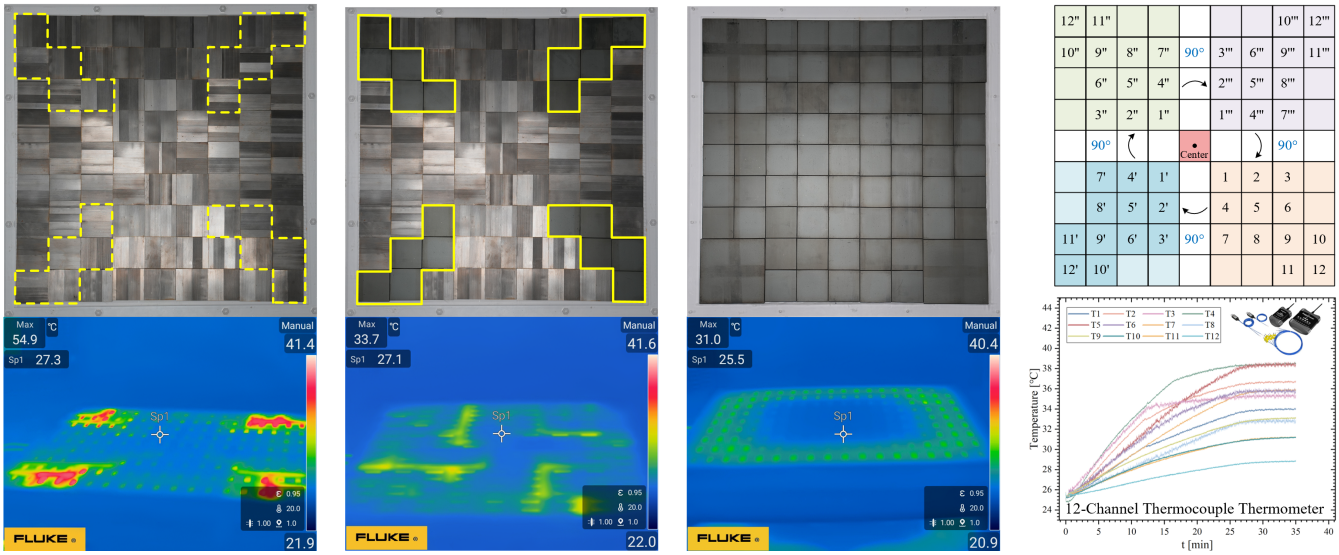

(a) (b) (c) (d)

Fig. 16. Thermal images captured by the Fluke TI300+ camera and temperature measurements obtained using the DagaSensor 12-channel thermocouple thermometer at 3.3 kW. (a) Case 3 after operating 10 min. (b) Case 3+ after operating 30 min. (c) Case 4 after operating 30 min. (d) Temperature measurement points and results for Case 3+.

has a 1.33 percentage point efficiency gap compared to the state-of-the-art full ferrite configuration (Case 4), our method effectively reflects the underlying differences in magnetic flux connectivity and uniformity. This leads to the conclusion that, to further improve the efficiency of NRC-dominated core plates, one can modify the stacking structure of the nanocrystalline cores to better guide magnetic flux paths. At the same time, special care must be taken to avoid the generation of eddy currents. Nevertheless, such structural modifications will inevitably increase the manufacturing cost of NRCs. Therefore, in practical applications, a balance among efficiency, weight, leakage flux, and manufacturing cost must be carefully considered.

C. Thermal Performance

Safe operation of IPT systems is crucial in high-power applications. Excessive heat generation and design mistakes can pose safety hazards, even leading to fire risks. By employing the proposed model and calculating MKI values, safety issues can be effectively avoided at the initial design stage, especially for designs using high-conductivity magnetic materials.

Fig. 16(a) shows the thermal image of Case 3 after 10 minutes of operation at 3.3 kW. Poor magnetic flux connectivity causes significant eddy current losses, raising the core surface temperature to 54.9 °C. Regions beneath the coil, especially near the four winding corners, experience the strongest magnetic fields and are highly sensitive to path discontinuities. These discontinuities cause localized flux crowding and thermal hotspots. Although nanocrystalline materials have a high Curie temperature, the bonding resin may ignite if the temperature exceeds a critical threshold, posing a fire risk.

In contrast, the optimized core structure in Case 3+ demonstrates improved thermal performance. After operating under the same 3.3 kW power level for 30 minutes, the maximum temperature recorded by the thermal camera drops observably to 33.7 °C, as shown in Fig. 16(b). This improvement is attributed to the added ferrite, which enhances the continuity of the magnetic path beneath the coil corners and suppresses eddy current concentration. The thermal performance of the isotropic full ferrite plate (Case 4) is further illustrated in Fig. 16(c), exhibiting excellent magnetic path connectivity and uniformity compared to anisotropic NRC cores.

It is important to note that thermal imaging accuracy depends on core material emissivity. For safety reasons, all images were captured from a distance of 1 m, potentially introducing deviations from ambient light. To obtain precise local temperatures, especially for Case 3+, a 12-channel thermocouple was used to measure the core surface directly. Twelve test points were strategically placed in one-quarter of the core plate, leveraging the symmetry of the magnetic field, as shown in Fig. 16(d). The highest temperature measured (38 °C) was observed at sensor positions 4 and 5, confirming that the thermocouple thermometer provided more accurate readings than the thermal camera.

These results show that MKI reflects magnetic path connectivity and uniformity for heterogeneous materials and highlights potential safety risks in high-power applications.

D. Coil Misalignment

Magnetic core distribution reshapes the magnetic field around the unipolar coils, affecting their power transfer performance. Figs. 17 and 18 illustrate the variations in dc-dc efficiency for four representative configurations under x- and z-directional misalignments at a 3.3 kW output, respectively.

In Case 1, the anisotropic nature of NRC significantly affects the transmission efficiency of the unipolar coils, both in aligned and misaligned conditions. After applying the proposed graph-based optimization to improve the connectivity and uniformity of magnetic flux paths, the magnetic flux can partially (Case 2+) or fully (Case 3+) penetrate the core plate

from the side. As a result, the dc-dc efficiency is notably improved when coil misalignment occurs.

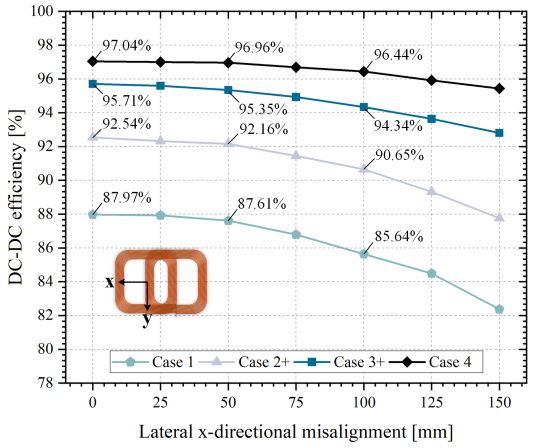

Fig. 17. DC-DC efficiency under *x*-direction misalignment.

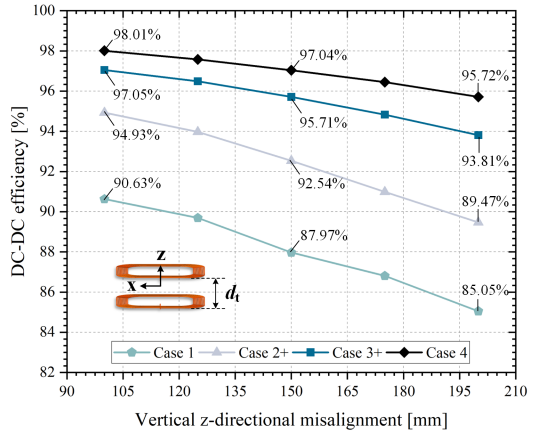

Fig. 18. DC-DC efficiency under *z*-direction misalignment.

It is worth noting that NRC-dominated cores, such as Case 1, Case 2+, and Case 3+, use an ultrathin 3 mm design with high saturation flux density, resulting in a smaller volume than 5 mm ferrite cores. Consequently, the coupling coefficient drops faster with misalignment, causing greater fluctuations in dc-dc efficiency. Designers must balance the reduced core weight and volume against the efficiency loss under positional offsets in practical applications.

E. Leakage Flux

Fig. 19 shows the simulated and measured magnetic flux density along the lateral *x*-direction, with error bars on the measured data indicating a $\pm 7\%$ uncertainty due to instrument precision and environmental factors. The simulation results show that Case 3+ exhibits lower spatial flux density across all ranges. To ensure safety and avoid exposure to strong magnetic fields, the flux density was evaluated only at a distance of 0.8 m from the center of the Rx coil, as specified by the SAE J2954 standard [31], using the Hioki FT3470-52 Magnetic Field HiTester. Benefiting from the high magnetic permeability of NRCs, the NRC-dominated core plate (Case 3+) achieves a 3 μT reduction in leakage flux, demonstrating better magnetic shielding capability compared to the full ferrite plate (Case 4).

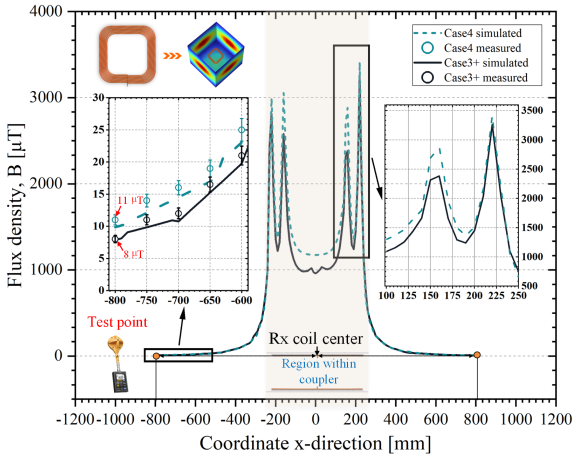

Fig. 19. Leakage flux comparison of Cases 3+ and 4 at 3.3 kW.

V. Discussion

Unlike conventional reluctance-based analyses [32], [33], [34], this work integrates the reluctance model with a graph-theoretic framework for planar magnetic core design. By introducing reluctance distance and MKI, the model evaluates magnetic flux connectivity in heterogeneous core plates for unipolar IPT coils. Leveraging graph representation, the optimized result highlights the potential of NRC as a lightweight, low-leakage alternative to ferrite. As summarized in Table III, the graph-optimized core configuration achieves significantly improved dc-dc efficiency for NRC-dominated IPT systems. For applications that do not require a fully covered magnetic core, the optimized results presented in this work are still applicable. By simply removing the cores at the center of the coil (see Fig. 20), the core weight and cost can be minimized while maintaining system efficiency.

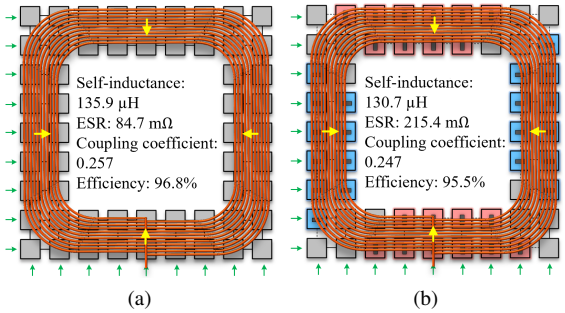

Fig. 20. Core-reduced designs. (a) Case 4 with 25 cores removed. (b) Case 3+ with 25 cores removed.

Although NRC materials offer high saturation flux density and tunable permeability, ferrite couplers still achieve higher transfer efficiency due to lower eddy-current losses. Thus, ferrite is preferred for efficiency-critical applications, NRC for weight- or space-constrained designs, and a hybrid ferrite-NRC structure can balance both advantages. To achieve a fully NRC core plate, specially crushed *z*-laminated NRCs can

TABLE III
COMPARISON OF THIS WORK WITH PREVIOUS MAGNETIC CORE DESIGNS FOR UNIPOLAR COILS

Literature	Core type	% of NRC**	Coil type	Distance	Power level	DC efficiency	Optimization method	Results**
[35]	Tx: ferrite 35*35*2 mm Rx: ferrite 35*35*2 mm	0%	Circular Tx: 35*35 mm Rx: 35*35 mm	N/A	N/A	96.50%	Neural network	Weight: ↓ 25.5%.
[36]	Tx: ferrite 500*400*12 mm Rx: ferrite 500*400*12 mm	0%	Rectangular Tx: 400*300 mm Rx: 270*195 mm	150 mm	3 kW	92.60%	Neural network	Weight: ↓ 10%.
[23]	Tx: hybrid 450*450*3/5 mm Rx: hybrid 450*450*3/5 mm	30%	Rectangular Tx: 224*224 mm Rx: 224*224 mm	150 mm	6.6 kW	96.97%	NSGA-II algorithm	Weight: ↓ 6.7%; B_{leakage}: ↓ 20%.
[26]	Tx: ferrite 650*500*5 mm Rx: NRC 330*330*5 mm	50%	Rectangular Tx: 650*500 mm Rx: 330*330 mm	150 mm	11 kW	94.04%	Varied permeability	Weight: ↓ 15.2%; Cost: ↑ 50%.
[25]	Tx: hybrid 500*500 mm Rx: hybrid 500*500 mm	50%	Rectangular Tx: 400*400 mm Rx: 400*400 mm	240 mm	1.5 kW	93.98%	Varied permeability	B_{leakage}: ↓ 5.3%.
[37]	Tx: NRC 200*200*2 mm Rx: NRC 200*200*2 mm	100%	Circular N/A	50 mm	3 kW	93.45%	Modified structure	Weight: ↓ 15.6%.
This work	Tx: hybrid 450*450*3/5 mm Rx: hybrid 450*450*3/5 mm	75%	Rectangular Tx: 224*224 mm Rx: 224*224 mm	150 mm	3.3 kW	95.71%	Graph theory	Weight: ↓ 16.3%; B_{leakage}: ↓ 27%; Cost: ↓ 39.1%.

* Area covered by NRCs for both Tx and Rx core plates; ** Compared before and after optimization in each work.

be used to replace ferrites. While this would inevitably raise manufacturing cost, it offers a feasible approach to further improve power density. In view of the representational capability of graphs, non-ferromagnetic materials can be incorporated into the graph-based model in the future to account for more complex magnetic designs.

VI. CONCLUSION

This paper proposes a graph-based optimization method to address the connectivity and uniformity challenges in anisotropic nanocrystalline ribbon cores for unipolar coils. By optimizing the proposed Magnetic Kirchhoff Index toward a desirable range, improvements in magnetic flux continuity, uniformity, and the figure of merit of the resonant network can be achieved. Experimental validation at 3.3 kW demonstrates that the optimized NRC structure outperforms the unidirectional stacking configuration, achieving a 7.74 percentage points improvement in efficiency. Compared with state-of-the-art ferrite design, the optimized NRC design achieves a 16.3% reduction in weight, a 27% decrease in leakage flux, and a 39.1% reduction in manufacturing cost. To further improve the performance of NRC-dominated magnetic core plates, future work may focus on customizing the shape of NRC elements to better guide magnetic flux pathways and refining the manufacturing process to minimize eddy current losses.

REFERENCES

[1] S. Y. Hui, "Planar wireless charging technology for portable electronic products and qi," *Proc. IEEE*, vol. 101, DOI 10.1109/JPROC.2013.2246531, no. 6, pp. 1290–1301, 2013.

[2] X. Yu, J. Feng, L. Zhu, and Q. Li, "Design and optimization of a planar omnidirectional wireless power transfer system for consumer electronics," *IEEE Open Journal of Power Electronics*, vol. 5, DOI 10.1109/OJPEL.2024.3360878, pp. 311–322, 2024.

[3] Y. Jiang, L. Wang, Y. Wang, J. Liu, X. Li, and G. Ning, "Analysis, design, and implementation of accurate zvs angle control for ev battery charging in wireless high-power transfer," *IEEE Transactions on Industrial Electronics*, vol. 66, DOI 10.1109/TIE.2018.2795523, no. 5, pp. 4075–4085, 2019.

[4] D. E. Gaona, C. Jiang, and T. Long, "Highly efficient 11.1-kw wireless power transfer utilizing nanocrystalline ribbon cores," *IEEE Transactions on Power Electronics*, vol. 36, no. 9, pp. 9955–9969, 2021.

[5] Y. Wang, C. Q. Jiang, X. Wang, L. Mo, W. Guo, and T. Long, "Laminated cores in inductive power transfer: A viaduct structure for balanced flux and minimal shielding loss," *IEEE Transactions on Power Electronics*, vol. 40, DOI 10.1109/TPEL.2025.3533697, no. 5, pp. 6464–6469, 2025.

[6] M. Wu, X. Yu, X. Yang, W. Chen, and L. Wang, "An efficiency optimization method for the multiple-coil wpt system against the pad misalignment," *IEEE Transactions on Transportation Electrification*, vol. 11, DOI 10.1109/TTE.2024.3410676, no. 1, pp. 1743–1753, 2025.

[7] J. Lu, G. Zhu, and C. C. Mi, "Foreign object detection in wireless power transfer systems," *IEEE Transactions on Industry Applications*, vol. 58, DOI 10.1109/TIA.2021.3057603, no. 1, pp. 1340–1354, 2022.

[8] H. Wang, Y. Zheng, Y. Zhou, Y. Wu, W. Pan, Z. Shen, X. Chen, X. Mao, and Y. Zhang, "Blind-zone-free metal object detection system for wireless ev charging system employing strip multipolar detection coils," *IEEE Transactions on Transportation Electrification*, vol. 11, DOI 10.1109/TTE.2024.3462439, no. 1, pp. 4420–4428, 2025.

[9] R. Zhang, Y. Wu, D. Zhao, Y. Li, Y. Jiang, Y. Tang, H. Yuan, X. Wang, and M. Rong, "Wireless power transfer system with automatic tuning capability in metallic environment," in *2025 IEEE Applied Power Electronics Conference and Exposition (APEC)*, DOI 10.1109/APEC48143.2025.10977115, pp. 3220–3226, 2025.

[10] B.-G. Choi and Y.-S. Kim, "New structure design of ferrite cores for wireless electric vehicle charging by machine learning," *IEEE Transactions on Industrial Electronics*, vol. 68, DOI 10.1109/TIE.2020.3047041, no. 12, pp. 12 162–12 172, 2021.

[11] Z. Li, X. Li, D. Yuan, J. Zhang, and Y. Liu, "Optimization of magnetic couplers in wireless charging systems using the surrogate model," *IEEE Journal of Emerging and Selected Topics in Power Electronics*, DOI 10.1109/JESTPE.2025.3544868, pp. 1–1, 2025.

[12] J. Ma, Z. Li, Y. Liu, M. Ban, and W. Song, "Thermal analysis and optimization of the magnetic coupler for wireless charging system," *IEEE Transactions on Power Electronics*, vol. 38, DOI 10.1109/TPEL.2023.3318356, no. 12, pp. 16 269–16 280, 2023.

[13] C. Chen, C. Jiang, Y. Wang, Y. Fan, B. Luo, and Y. Cheng, "Compact curved coupler with novel flexible nanocrystalline flake ribbon core for autonomous underwater vehicles," *IEEE Transactions on Power Electronics*, vol. 39, DOI 10.1109/TPEL.2023.3322466, no. 1, pp. 53–57, 2024.

[14] J. Xiang, C. Q. Jiang, T. Ma, Y. Wang, and Y. Fan, "An ultra-thin self-resonant coupler with nanocrystalline flake ribbons for wireless power transfer system," *IEEE Transactions on Magnetics*, vol. 60, DOI 10.1109/TMAG.2024.3429488, no. 9, pp. 1–5, 2024.

[15] Z. Luo, X. Li, C. Jiang, Z. Li, and T. Long, "Permeability-adjustable nanocrystalline flake ribbon in customized high-frequency magnetic components," *IEEE Transactions on Power Electronics*, vol. 39, DOI 10.1109/TPEL.2023.3341797, no. 3, pp. 3477–3485, 2024.

[16] J. Xiang, C. Q. Jiang, T. Ma, Y. Wang, and Y. Fan, "An ultra-thin self-resonant coupler with nanocrystalline flake ribbons for wireless power transfer system," *IEEE Transactions on Magnetics*, vol. 60, DOI 10.1109/TMAG.2024.3429488, no. 9, pp. 1–5, 2024.
[17] Y. Wu, Y. Jiang, Y. Li, H. Yuan, X. Wang, and Y. Tang, "Precise parameterized modeling of coil inductance in wireless power transfer systems," *IEEE Transactions on Power Electronics*, vol. 39, DOI 10.1109/TPEL.2024.3389746, no. 9, pp. 11 746–11 757, 2024.
[18] Y. Li, Y. Jiang, Y. Wu, Z. Yao, X. Yu, X. Wang, Z. Liao, and Y. Tang, "A universal parameter design method of resonant coils under multiple boundary constrains for wireless power transfer systems," in *2023 IEEE Energy Conversion Congress and Exposition (ECCE)*, DOI 10.1109/ECCE53617.2023.10362919, pp. 6489–6496, 2023.
[19] B. S. Gu, T. Dharmakeerthi, S. Kim, M. J. O'Sullivan, and G. A. Covic, "Optimized magnetic core layer in inductive power transfer pad for electric vehicle charging," *IEEE Transactions on Power Electronics*, vol. 38, no. 10, pp. 11 964–11 973, 2023.
[20] A. K. Bailey, W. Zhang, S. Kim, and G. A. Covic, "Anisotropic characterization of nanocrystalline alloys for inductive power transfer," *IEEE Open Journal of Power Electronics*, vol. 5, DOI 10.1109/OJPEL.2024.3510641, pp. 1830–1841, 2024.
[21] Y. Wang, C. Q. Jiang, C. Chen, X. Wang, X. Li, and T. Long, "Design and analysis of inductive power transfer system using nanocrystalline flake ribbon core," *IEEE Journal of Emerging and Selected Topics in Power Electronics*, vol. 12, DOI 10.1109/JESTPE.2024.3358857, no. 4, pp. 3334–3347, 2024.
[22] Y. Li, S. Wang, Y. Wu, Y. Jiang, X. Zhu, Z. Xiao, Z. He, and Y. Tang, "A novel hybrid magnetic core design method for weight reduction of wireless power transfer systems," in *2024 IEEE Applied Power Electronics Conference and Exposition (APEC)*, DOI 10.1109/APEC48139.2024.10509336, pp. 1202–1206, 2024.
[23] Y. Li, S. Wang, Y. Wu, Y. Jiang, Z. Xiao, and Y. Tang, "Heterogeneous integration of isotropic and anisotropic magnetic cores for inductive power transfer," *IEEE Transactions on Power Electronics*, vol. 40, DOI 10.1109/TPEL.2024.3485193, no. 2, pp. 3770–3784, 2025.
[24] A. Wadsworth, M. G. Pearce, D. J. Thrimawithana, and L. Zhao, "Dense and efficient cryogenic power converter using stress annealed and stacked nanocrystalline cores," *IEEE Transactions on Power Electronics*, vol. 40, DOI 10.1109/TPEL.2024.3491037, no. 2, pp. 3357–3369, 2025.
[25] W. Zhang, Q. Yang, Y. Li, Z. Lin, M. Yang, and M. Mi, "Comprehensive analysis of nanocrystalline ribbon cores in high-power-density wireless power transfer pads for electric vehicles," *IEEE Transactions on Magnetics*, vol. 58, no. 2, pp. 1–5, 2022.
[26] M. Xiong, X. Wei, Y. Huang, Z. Luo, and H. Dai, "Research on novel flexible high-saturation nanocrystalline cores for wireless charging systems of electric vehicles," *IEEE Transactions on Industrial Electronics*, vol. 68, DOI 10.1109/TIE.2020.3016259, no. 9, pp. 8310–8320, 2021.
[27] K. Thulasiraman, M. Yadav, and K. Naik, "Network science meets circuit theory: Resistance distance, kirchhoff index, and foster's theorems with generalizations and unification," *IEEE Transactions on Circuits and Systems I: Regular Papers*, vol. 66, DOI 10.1109/TCSI.2018.2880601, no. 3, pp. 1090–1103, 2019.
[28] D. J. Klein and M. Randic, "Resistance distance," *Journal of Mathematical Chemistry*, vol. 12, no. 1, pp. 81–95, 1993.
[29] TDK, "Ferrites and accessories siferrit material n95." [Online]. Available: https://www.tdk-electronics.tdk.com/download/187222/d2caba056c7aa06d1e24ece60fb6ed5e/pdf-n95.pdf
[30] Antai, "Nanocrystalline ribbons." [Online]. Available: https://www.antai-emarketing.com/nanocrystalline-ribbon/
[31] Society of Automotive Engineers International, *Wireless Power Transfer for Light-Duty Plug-In/Electric Vehicles and Alignment Methodology*. SAE International, 2019.
[32] M. Cheng, Z. Xu, and G. Zhang, "Vector magnetic circuit based equivalent magnetic network for flux-switching permanent magnet machines," *IEEE Transactions on Energy Conversion*, vol. 40, DOI 10.1109/TEC.2024.3467949, no. 2, pp. 1517–1528, 2025.
[33] A. M. Silva, C. H. Antunes, A. M. S. Mendes, and F. J. T. E. Ferreira, "Generalized reluctance network framework for fast electromagnetic analysis of radial-flux machines," *IEEE Transactions on Energy Conversion*, vol. 38, no. 1, pp. 310–320, 2023.
[34] L. Wang, S. Zhang, W. Cai, B. Li, Z. Zhan, N. Bianchi, and A. Boglietti, "A novel multistructure equivalent magnetic network model for pmsm with enhanced magnetic field analysis and saturation compensation," *IEEE Transactions on Transportation Electrification*, vol. 11, DOI 10.1109/TTE.2025.3581178, no. 5, pp. 11 692–11 700, 2025.
[35] Fawad, S. A. A. Shah, Y. Park, and Y.-S. Kim, "Machine learning-driven joint structuring of wpt coil and core for enhanced mutual inductance and reduced ferrite volume," *IEEE Transactions on Power Electronics*, vol. 40, no. 10, pp. 15 880–15 890, 2025.
[36] B.-G. Choi and Y.-S. Kim, "New structure design of ferrite cores for wireless electric vehicle charging by machine learning," *IEEE Transactions on Industrial Electronics*, vol. 68, DOI 10.1109/TIE.2020.3047041, no. 12, pp. 12 162–12 172, 2021.
[37] D. Wang, S. Cui, J. Zhang, Z. Bie, R. Lu, and C. Zhu, "A novel diagonal-laminated fe-based nanocrystalline ribbon core structure in wireless power transfer systems," in *2024 IEEE 7th Student Conference on Electric Machines and Systems (SCEMS)*, DOI 10.1109/SCEMS63294.2024.10756367, pp. 1–6, 2024.

Yaohua Li (Graduate Student Member, IEEE) received the B.Eng. degree in electrical engineering from University of Calgary, Calgary, Canada, in 2020, and the M.Sc. degree in power engineering in 2021 from Nanyang Technological University, Singapore, where he is currently pursuing the Ph.D. degree in electrical engineering.

His research interests include wireless power transfer, high-frequency magnetics, robotics and artificial intelligence.

Sicheng Wang (Student Member, IEEE) received the B.Eng. degree in energy and power engineering from North China Electric Power University, China, in 2022, and the M.Sc. degree in power engineering in 2024 from Nanyang Technological University, Singapore.

In 2024, he joined the China Electrical Power Research Institute, China, where his research interests include wireless power transfer and advanced magnetic design.

Delin Zhao (Graduate Student Member, IEEE) received the B.E. degree from Jilin University in 2020 and M.E. degree from Xi'an Jiaotong University in 2023, both in electrical engineering. Currently, he is working toward PhD degree at Nanyang Technological University, Singapore.

His main research interests include modeling and control of wireless power transfer systems.

Shuxin Chen (Member, IEEE) received the B.Eng. degree in electronic engineering from the Hong Kong Polytechnic University, Hong Kong, in 2015, the bachelor's degree in microelectronic engineering from Sun Yet-Sen University, Guangzhou, China, in 2015, and the M.Sc. degree in power engineering and the Ph.D. degree in electrical engineering from Nanyang Technological University, Singapore, in 2016 and 2021, respectively. From 2022 to 2023, he was a Research Fellow with Nanyang Technological University, Singapore. Since 2023, he has been a Senior Engineer at Dyson Singapore.

His current research interests include wireless power transfer and power converter design and control.

Yongbin Jiang (Member, IEEE) received the B.S. degree in electrical automatization from Jiangsu University, Zhenjiang, China, in 2012, and the M.S. degree in instrument science and technology and the Ph.D. degree in electrical engineering from Xi'an Jiaotong University, Xi'an, China, in 2016 and 2020, respectively. From 2020 to 2022, he worked as the director of Digital Energy Laboratory of the UNISOC (Shanghai) Technologies Co., Ltd, in Shanghai, China. Since 2022, he has been a Research Fellow with Nanyang Technological University, Singapore.

His research interests include wireless power transfer, high frequency and high-power density dc/dc converters, and digital control technology.

Zhigang Yao (Senior Member, IEEE) received the B.S. and Ph.D. degrees in electrical engineering from Chongqing University, Chongqing, China, in 2014 and 2020, respectively. From 2022 to 2025, he was a Research Fellow with the Energy Research Institute, Nanyang Technological University, Singapore. He is currently an Associate Professor with the School of Electrical Engineering, Chongqing University, Chongqing, China. He first proposed the trapezoidal current mode (TZCM) for multilevel converters to achieve ZVS while reducing peak current.

His current research interests include high power multiphase/multilevel dc-dc converters, three-level inverters, resonant converters, and ZVS soft-switching techniques.

Yi Tang (Senior Member, IEEE) received the B.Eng. degree in electrical engineering from Wuhan University, Wuhan, China, in 2007, and the M.Sc. and Ph.D. degrees in electrical engineering from the School of Electrical and Electronic Engineering, Nanyang Technological University, Singapore, in 2008 and 2011, respectively. From 2011 to 2013, he was a Senior Application Engineer with Infineon Technologies Asia Pacific, Singapore. From 2013 to 2015, he was a Postdoctoral Research Fellow with Aalborg University, Aalborg, Denmark. Since March 2015, he has been with Nanyang Technological University, where he is currently a tenured Associate Professor and serves as Associate Chair (Graduate Studies). His research interests include power electronics and its applications in smart grid and e-mobility systems.

Dr. Tang was the receipt of the Infineon Top Inventor Award in 2012, Early Career Teaching Excellence Award in 2017, and four IEEE Prize Paper Awards. He serves as an Associate Editor for IEEE Transactions on Power Electronics and IEEE Journal of Emerging and Selected Topics in Power Electronics.